Jahn-Teller effect with rigid octahedral rotations in perovskites

Rukhshanda Naheed, M. Ahsan Zeb,[*] and Kashif Sabeeh
Department of Physics, Quaid-i-Azam University, Islamabad 45320, Pakistan

We consider rigid rotation and tilting of the anion octahedra around the transition metal ions in ABO$_3$ perovskites from the viewpoint of the Jahn-Teller problem and study the effect of the crystal field of the nearest A and B ion cages on the single electron spectrum of the central transition metal B ions. While the crystal field of the octahedra, which creates degenerate manifolds e_g and t_{2g}, does not change with such rigid rotations, the field of A and B cages deforms significantly from the ideal octahedral field in a way that leads to sizable splittings in these manifolds. The lowering of the ground state energy of a given many-electron configuration due to these splittings can thus be an important driving force behind the octahedral rotations and associated structural transformations. We find that the size of the splitting and the order of the orbitals are determined by a competition between the A and B cages, as well as a competition between the tilt and rotation angles.

I. INTRODUCTION

Perovskites exhibit a rich variety of intriguing electronic, magnetic and optical properties [1–7] due to the interplay between spin, orbital, and structural degrees of freedom and widely varying electronic correlations. These materials are important both for practical applications in all sorts of modern devices and fundamental understanding of various physical phenomena [8–12].

The perovskite structures have a common formula unit ABX_3, where A and B are positive ions while X are negative ions that form octahedra around B. In a cubic perovskite, the octahedra are symmetric, but they can distort [13–18] or simply rotate [19–25] to lower the symmetry and produce, e.g., a rhombohedral, tetragonal or orthorhombic structure. Octahedral rotations also occur in other perovskite related structures and have been extensively studied due to their crucial role in determining various physical properties, e.g., in ferroelectric [26–33] and multiferroic [34–41] systems. The interplay of octahedral rotations and spin-orbit coupling [42,43], breathing distortions [44], strain [45], defects [46], and pressure [47], and their role in magnetostructural phase transitions [48], orbital order [49,50], orbital anisotropy [51], and surface electronic structure [52], have also been investigated. Since, usually, the octahedra are not just distorted or rotated but a combination of both, the influence of these two structural mutations on each other has recently been explored by many authors [18,50,53] as well.

While the tetragonal distortion of the octahedra is associated with a (cooperative) Jahn-Teller effect [13–18,54–60] (i.e., the orbital degeneracy of the metal ion coordinated by the anionic octahedron is lifted, which stabilizes the distortion), the rotation and tilting of the octahedra are almost always explained empirically in terms of the relative sizes of the three ions with the Goldschmidt tolerance factor [61,62].

Based on density functional theory (DFT) calculations, a few recent works [63–66], however, suggest that the octahedral rotation and tilting is a second order Jahn-Teller effect [67–72] (i.e., the distortion is stabilized by a coupling between the ground and excited adiabatic potential energy surfaces). Garcia-Fernandez *et al.* study potassium fluoride perovskite family KMF$_3$ ($M = $ Ca^{2+} or a $3d$ transition metal) and found that the tilting angle depends on the covalent bonding through the mixing of occupied and low-lying unoccupied orbitals of the transition metal [63]. Cammarata and Rondinelli find a negative correlation between metal-oxygen bond covalency and octahedral rotation in orthorhombic perovskite oxides [64]. Lee *et al.* find similar results for metal-iodine bonding in lead iodide perovskites, where the role of the hydrogen bonding in a hybrid perovskite with organic ammonium ions at A sites is also found to be crucial [65]. Yoshida *et al.* use DFT along with representation theory analysis and indicate that the rotations are induced by bonding interaction between the valence and conduction band Bloch states at different wave vectors that are mapped onto each other on Brillouin zone folding for the associated lattice distortion [66].

We take a completely different approach to this problem. We go back to the basics and see what is it that lifts the orbital degeneracy in the classical JT effect? It is a specific deformation of the crystal field at the transition metal (JT ion) site. Does the same happen in the case of octahedral tilting and rotations? While the potential of an octahedral anion cage in its own frame does not change with rigid rotations for obvious reason, the total crystal field does deform because the rest of the lattice is not only rotated in a given octahedron's frame (that turns its nonspherical potential) but also distorted owing to the accompanying structural transformation. Using this insight and elements of crystal field theory [59,73,74], we consider next two coordination cages around an octahedron and find that, just like a first order JT effect, the deformed crystal field in this case also lifts the orbital degeneracy, by a significant amount for typical system parameters, signalling the instability against the rotations.
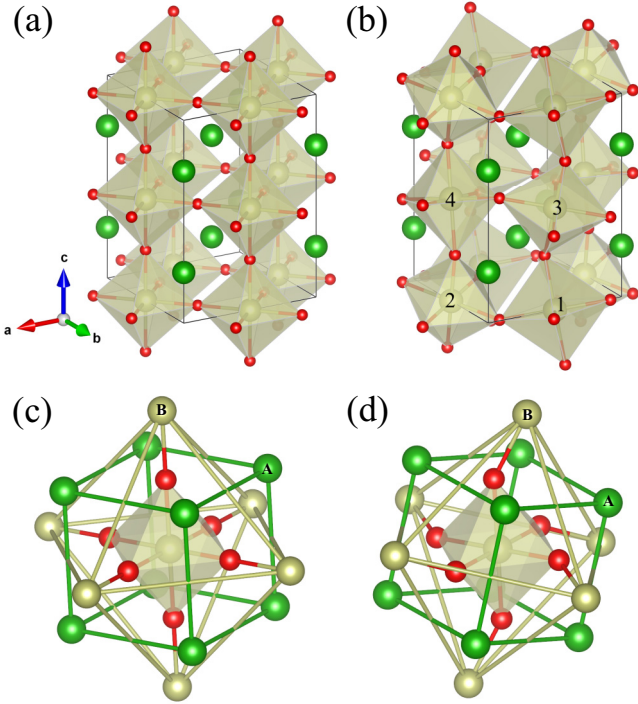
*ahsan.zeb@hotmail.com

FIG. 1. Crystal structures and coordination cages. Crystal structures of cubic (a) and orthorhombic (b) perovskites. The anions (red) form the shown octahedra around the B cations (gold), while the A cations (green) sit in the voids between the octahedra. In the orthorhombic structure shown here (b), the octahedra are rotated and tilted by $15°$. [(c) and (d)] The coordination cages of A and B cations just next to the anion octahedron around a B ion in cubic and orthorhombic perovskites. In the anion octahedron's frame, the cages are symmetric and aligned to the octahedron in the cubic perovskites (c), while they are rotated and slightly distorted in the orthorhombic perovskites (d).

Since the octahedra are connected to each other (making a three-dimensional network in the perovskite structure), rotating one octahedron rotates all other in the crystal in a consistent fashion [19]; see Figs. 1(a) and 1(b). We consider an octahedral *rotation* β around 001 direction (that transforms the structure from cubic $Pm\bar{3}m$ to tetragonal $P4/mbm$) followed by a *tilting* α around the new 110 direction (transforming to orthorhombic $Pbnm$, or $Imma$ at $\beta = 0$). We use the rotation and tilt terminology for these two angles throughout the rest of the manuscript.

Beyond the anion octahedron, each transition metal ion B in a cubic perovskite is coordinated by two cation cages, a cube of A and an octahedron of B, as shown in Figs. 1(c) and 1(d). Including the potential of these two ion cages into the crystal field Hamiltonian of the central ion B, we explore the effect of the rotation and tilting on its t_{2g} and e_g manifolds that are created primarily by the anion's octahedral potential. We find that the degeneracy of t_{2g} and e_g is lifted. The size of the splitting and the order of the orbitals depend on the relative charges on the two types of cations and a competition between rotation and tilting. At typical parameter values, the splitting is large enough to play a major role in the corresponding structural instability. The qualitative picture developed by our

calculations holds even when the potential of the full lattice is considered.

The paper is organized as follows. Section II presents the formalism and Sec. III reviews the Jahn-Teller effect to introduce the notation and concepts involved by considering tetragonal distortion of an octahedron. The model and calculations are presented in Sec. IV, where we first discuss the relative contributions of the three closest ion cages in the cubic structure to the crystal field at the central transition metal site and crystal field splitting between its e_g and t_{2g} manifolds (Sec. IV A), and then describe the deformation effects of rigid octahedral rotations on the structure (Sec. IV B) and crystal field (Sec. IV C). The results are in Sec. V, where we present the splitting in the single particle spectrum belonging to the t_{2g} (Sec. V A) and e_g (Sec. V B) manifolds, and finally describe the effect of the full lattice (Sec. V C).

II. FORMALISM: CRYSTAL FIELD HAMILTONIAN USING MULTIPOLE EXPANSION OF THE CRYSTAL FIELD POTENTIAL

Let us introduce the basic formalism we use throughout this manuscript. The spectrum of an atom or ion changes in the presence of nearby charged species. This is described by the crystal field Hamiltonian of the atom that contains the coupling between its atomic orbitals and/or their energy shifts induced by the electrostatic potential of those charges. Since the angular part of atomic orbitals are described by the spherical harmonics, an expansion of the potential at the atom's site in the same bases simplifies the analysis. This is because the effect of various multipole components of the potential is governed by certain selection rules (enforced by the symmetries of the spherical harmonics through Gaunt coefficients, see below).

If we have an arrangement of ions with charge q around a given site, we can express their potential in terms of spherical harmonics [59],

$$V(\vec{r}) = \frac{q}{a} \sum_{lm} V_{lm} \left(\frac{r}{a} \right)^l Y_{lm}(\hat{r}), \qquad (1)$$

where a sets the length scale, $\hat{r} = \vec{r}/r$ is the direction of $\vec{r}$, and $V_{l,m}$ are multipole components of the potential (for the given site as origin and a chosen orientation). Assuming we have a transition metal atom/ion at the central site with only d orbitals ($l = 2$), the matrix elements of its crystal field Hamiltonian are then given by

$$H_{m'm''} = -\frac{q}{a} \sum_{l,m} V_{lm} C_l^{m'm''m} D_l, \qquad (2)$$

where $C_l^{m'm''m} = \langle Y_{2m'} | Y_{lm} | Y_{2m''} \rangle$ are Gaunt coefficients for the given (real or complex) spherical harmonics, and $D_l = \langle (r/a)^l \rangle$ is the expectation of $(r/a)^l$ evaluated in the d-orbital bases assuming the same radial dependence for all orbitals [75]. The sum is restricted to even values of $l \leqslant 4$ as $C_l^{m'm''m} = 0$ otherwise, with $-l \leqslant m \leqslant l$.

We consider transition metal oxides as an example perovskite system throughout the rest of the manuscript, but our calculations and results are general and also apply to

perovskite transition metal compounds with other anions, e.g., halides and chalcogenides.

A. Atom/ion in an octahedral field: t_{2g} and e_g manifolds

Consider six oxygen (O) ions each with a charge $-q_o$ making an octahedron of size a (where these anions are placed at the face centres of a cube of edge length a). The nonspherical part of the potential they produce at the center of the octahedron relevant for the d orbitals contains only two $l = 4$ components, in a specific ratio ($V_{4,0} : V_{4,4} = 1 : \sqrt{5/7}$), and is called octahedral field. It is given by [59]

$$V_{\text{oct}}(\vec{r}) = -\frac{224\sqrt{\pi}}{3}\frac{q_o}{a}\left(\frac{r}{a}\right)^4\left[Y_{4,0}(\hat{r}) + \sqrt{\frac{5}{7}}Y_{4,4}(\hat{r})\right]. \quad (3)$$

The crystal field Hamiltonian of a transition metal ion B in the field $V_{\text{oct}}(\vec{r})$ turns out to be diagonal, with its states split into two manifolds: $H_{mm} = -\Delta/3$ for $m \in \{-2, -1, 1\}$ (xy, yz, zx orbitals) called t_{2g}, and $H_{mm} = +2\Delta/3$ for $m \in \{2, 0\}$ ($x^2 - y^2$, z^2 orbitals) called e_g. The crystal field splitting between the two manifolds is $\Delta = \frac{160}{3}\frac{q_o}{a}D_4$.

III. JAHN-TELLER EFFECT

The Jahn-Teller effect [13–18,54–60] describes the geometric and electronic instability of a molecule, cluster or crystal with a symmetric structure and orbitally degenerate ground state against structural distortions. The distortions reduce the symmetry of the structure and lift the electronic degeneracy. This lowers the energy of the system proportional to the distortion. The elastic energy of the structure that increases as the square of the distortion competes with this linear term and the optimum structure is obtained at a finite distortion, as described below.

The dependence of the elastic energy on the distortion can be roughly explained as follows. Consider an elongation or a compression of an octahedron along one of its axes by $a\delta$, where a is the size of the octahedron and lattice constant of the cubic perovskite structure. The corresponding change in the unit cell volume would be linear in δ as $\sim a^3\delta$ so the elastic energy would change as $\sim\delta^2$. Assuming a linear change in the electronic spectrum, the total energy has a form $E = -\rho\delta + K\delta^2$, where ρ and K are positive constants describing the changes in the electronic and elastic energies, and would be optimum at $\delta = \rho/2K$. In general, as long as the two competing terms are not the same degree monomial in the distortion, the ground state can have a finite distortion. We use this argument to focus only on the changes in the electronic energy throughout this paper.

It is worth reminding that, in the Jahn-Teller problem, we usually consider single particle spectrum, i.e., single electron energy states, to analyze the ground state of a many electron system, which is the lowest energy "electronic configuration" (a combination of occupied single particle states out of all available single particle states, or a slater determinant of that combination to be more precise!). So a degenerate set of states that are completely occupied makes a nondegenerate many electron state because only a single configuration/combination is possible. For a given number of electrons in the d shell of the transition metal ion, we can determine the (most likely)

configuration(s) or ground state(s) using Hund's rule and see if it is degenerate or otherwise.

In the following, we consider an octahedral environment around a transition metal ion and illustrate how the changes in the electronic energy can be calculated when the octahedron is elongated.

A. Tetragonal distortion of an octahedron

Let us consider elongation of an octahedron along one of its O-B-O bonds. Align the Cartesian axes along O-B-O bonds and stretch the two bonds along z axis equally by an amount $a\delta$. The potential $V^{JT}(\vec{r})$ at the central B site (JT ion) of this deformed octahedron still contains only a few nonzero components (see Appendix for a method to calculate V_{lm}^{JT}). Not only the ratio $V_{4,0}^{JT} : V_{4,4}^{JT}$ now deviates from ideal octahedral field in Eq. (3), there is an $l = 2$ component induced due to the deformation,

$$V_{2,0}^{JT} = -\frac{32\sqrt{\frac{\pi}{5}}\delta(\delta^2 + 3\delta + 3)}{(\delta + 1)^3}, \quad (4)$$

$$V_{4,0}^{JT} = \frac{32}{3}\sqrt{\pi}\left(\frac{4}{(\delta + 1)^5} + 3\right), \quad (5)$$

$$V_{4,4}^{JT} = \frac{32\sqrt{35\pi}}{3}. \quad (6)$$

The crystal field Hamiltonian of the JT ion, $H_{m'm''}^{JT} = (q_o/a)\sum_{l,m}V_{lm}^{JT}C_l^{m'm''m}D_l$, still turns out to be diagonal (i.e., the deformation δ will not couple these orbitals to each other), but the degeneracies of the two manifolds is lifted and their respective average energies also shifted. Defining $F_n(\delta) = 1 - 1/(1 + \delta)^n$, we see that the t_{2g} now splits into two levels, with energies

$$E_{xy} = \frac{32}{7}\frac{q_o}{a}\left(D_2F_3 - \frac{20}{9}D_4F_5\right), \quad (7)$$

$$E_{yz} = E_{zx} = -\frac{1}{2}E_{xy}, \quad (8)$$

as measured from their average $E_0^{t_{2g}} = -64q_oD_4(3 - F_5)/9a$. Similarly, e_g splits up as

$$E_{x^2-y^2} = \frac{32}{7}\frac{q_o}{a}\left(D_2F_3 + \frac{5}{3}D_4F_5\right), \quad (9)$$

$$E_{z^2} = -E_{x^2-y^2}, \quad (10)$$

as measured from their average $E_0^{e_g} = 32q_oD_4(3 - F_5)/3a$. The crystal field splitting becomes $\Delta \equiv E_0^{e_g} - E_0^{t_{2g}} = 160q_oD_4(3 - F_5)/9a$. At small δ, expanding F_3, F_5 up to first order in δ, we obtain

$$(E_{xy}, E_{yz}, E_{zx}) = (2, -1, -1)\left[D_2 - \frac{100}{27}D_4\right]\frac{48}{7}\frac{q_o}{a}\delta, \quad (11)$$

$$(E_{x^2-y^2}, E_{z^2}) = (1, -1)\left[D_2 + \frac{25}{9}D_4\right]\frac{96}{7}\frac{q_o}{a}\delta, \quad (12)$$

whereas $E_0^{t_{2g}}$, $E_0^{e_g}$, and Δ all are rescaled by a factor of $1 - 5\delta/3$.

The terms in square brackets on the right of Eqs. (11) and (12) contain D_2 and D_4. D_4 is proportional to the crystal

field splitting Δ ($D_4 = \frac{3a}{160q_o}\Delta$) and we can estimate its value from realistic values of Δ for a given octahedron of size a and ion charge $-q_o$. Assuming $a = 7.0$ bohr and $q_o = 2e$ (e being the elementary charge), D_4 ranges from 1×10^{-3} to 7×10^{-3} for $\Delta \simeq 0.5$–3 eV. Typically, $D_2 \approx \sqrt{D_4}$, so $D_2/D_4 \approx 1/\sqrt{D_4}$ and it roughly ranges between 29 and 12 for D_4 in the above range. This means that, for realistic systems, we should always have $D_2/D_4 > 100/27$, $25/9 \approx 4$ so D_2 terms in Eqs. (11) and (12) dominate and determine the sign and size of the splittings.

So far, we have calculated the changes in the single particle energy levels of the B ion. Whether the deformation would be energetically favourable or not will depend on the number of electrons occupying these levels, as illustrated below.

Let us consider a JT/B ion with two electrons. In the symmetric octahedron case, we will have a degenerate (many electron) ground state with both electron in the same spin state (Hund's rule) in the t_{2g} manifold. Distorting the structure $\delta > 0$, we lower the ground state energy because we can now choose yz, zx orbitals that have lower energy than the original t_{2g} energy of the undistorted structure. In case of a JT/B ion with three electrons, the situation is very different. Assuming Hund's coupling is enough to still produce complete spin polarization, there is only one possible orbital configuration, one electron in each of xy, yz, zx orbitals. This nondegenerate (many electron) ground state does not lower its energy if the structure is distorted because the gain due to yz, zx is already balanced by the loss due to picking the higher energy xy state.

To complete the discussion of the JT instability, it is worth mentioning that JT effect occurs in all kinds of systems—molecules, clusters and crystals. In crystals, e.g., perovskites, it becomes a cooperative effect where the elongation of one octahedron is accompanied by a compression of adjacent octahedron, which minimizes the changes in the unit cell volume and hence the elastic energy cost of the transformation. Such alternate elongations and compressions also lead to an interesting long range orbital ordering where alternate orbitals are populated on the adjacent JT sites.

IV. MODEL AND CALCULATIONS OF ABO$_3$ PEROVSKITES

We now turn to our model and calculations of the splittings in the t_{2g} and e_g manifolds due to the deformations in the crystal field that are produced as the octahedra rotate or tilt. First, let us consider the cubic perovskite and see how much A and B cages contribute to the octahedral crystal field and associated splitting Δ between t_{2g} and e_g manifolds.

A. Contribution of different coordination cages in a cubic perovskite

In a cubic perovskite ABO$_3$, each transition metal atom/ion B is surrounded by six O^{2-}, each at a distance $a/2$, making an octahedron of size a around it. The potential of these ions $V_O(\vec{r}) = V_{\text{oct}}(\vec{r})$ splits the degenerate d orbitals by an amount $\Delta_o = 160q_oD_4/3a$ into t_{2g} and e_g. However, this is not the only crystal field potential at the B site. The coordination cages of next nearest neighbors, eight A atoms/cations all at the same distance $\sqrt{3}a/2$ make a cube around the B ion, which

also produces an octahedral field, given by

$$V_A(\vec{r}) = \frac{8}{81\sqrt{3}}\frac{q_A}{q_o}V_O(\vec{r}). \tag{13}$$

Furthermore, the nearest neighboring B ions, six of them each at a distance a, make an octahedron, with a potential

$$V_B(\vec{r}) = -\frac{1}{32}\frac{q_B}{q_o}V_O(\vec{r}). \tag{14}$$

It is interesting to note that $V_A(\vec{r})$ and $V_B(\vec{r})$ have opposite signs and their combined effect $V_{AB}(\vec{r}) = V_A(\vec{r}) + V_B(\vec{r})$ depends on their relative charges. Using the charge neutrality $q_B = 3q_o - q_A$ (remember that we take anion charge to be $-q_o$), we can write

$$V_{AB}(\vec{r}) = f_{q_A}V_O(\vec{r}), \tag{15}$$

$$f_{q_A} = \left(\frac{1}{32} + \frac{8}{81\sqrt{3}}\right)\frac{q_A}{q_o} - \frac{3}{32}, \tag{16}$$

which shows that $V_{AB}(\vec{r})$ vanishes at $q_A/q_o = 729/(256\sqrt{3} + 243) \simeq 1.062$.

Including the contribution of these AB cages to the crystal field, we obtain

$$V(\vec{r}) = (1 + f_{q_A})V_O(\vec{r}), \tag{17}$$

whereas the splitting becomes $\Delta = (1 + f_{q_A})\Delta_o$. We see that, relative to the O octahedron, the contribution of the two cation cages towards the total field splitting is relatively small at any q_A but still too large to be ignored. It can be measured by $(\Delta - \Delta_o)/\Delta_o = f_{q_A}$, which linearly changes from $-3/32 \simeq -10\%$ at $q_A = 0$ to $8/27\sqrt{3} \simeq 17\%$ at $q_A = 3q_o$. Typical values of q_A relevant for real transition metal oxides can be safely assumed to range between 0 and 4; $q_A = 0$ for systems like tungsten oxide WO_3 that do not have any cations at the A sites, and $q_A = 4$ still contributing just above 8%. We will see that, as the anion octahedra rotate or tilt, $V_{AB}(\vec{r})$ rotate in its frame and deform as well. The deformation also induces $l = 2$ components, which couple to the d orbitals of the B ion much more strongly.

B. Rigid octahedral rotations: transformation of the crystal structure

We consider a $\sqrt{2} \times \sqrt{2} \times 2$ unit cell of the cubic structure that transforms to the unit cell of the orthorhombic structure under octahedral rotation and tilting, as shown in Fig. 1. Assuming $\mathbf{a}, \mathbf{b}, \mathbf{c}$ to be the lattice vectors, two B atoms in a layer are situated at $\mathbf{a}/2, \mathbf{b}/2$, while two A atoms in the same layer are at $\mathbf{c}/4, (\mathbf{a} + \mathbf{b})/2 + \mathbf{c}/4$. Similar atoms in the second layer are simply shifted by $\mathbf{c}/2$. While the lattice vectors change under the rotation and tilting of the octahedra, these relations do not change. The O atoms in the cubic structure lie half way between the B atoms and make octahedral cages around them. Their positions in the deformed structure are not directly required for our calculations and discussion.

We rotate the octahedra by an angle β about $\hat{z} \equiv 001$ and then tilt it about the new 110 by an angle α [76]. The four octahedra in the cell have to be rotated and tilted clockwise or counter clockwise consistently. For example, (α, β), $(-\alpha, -\beta)$, $(-\alpha, \beta)$, $(\alpha, -\beta)$ for the octaherda labeled 1

through 4 in Fig. 1(b). The structure transforms from cubic to orthorhombic under these rotation and tilting of the octahedra. The lattice vectors of the deformed structure and the positions of A and B atoms can be calculated easily by calculating the coordinates of all six oxygen atoms that make the octahedra (by rotating and tilting the octahedra) for all four octahedra in the unit cell and comparing the coordinates of their shared oxygen atoms. We obtain

$$\begin{pmatrix} \mathbf{a} \\ \mathbf{b} \\ \mathbf{c} \end{pmatrix} = a \begin{pmatrix} \cos\beta & \cos\beta & 0 \\ -\cos\alpha\cos\beta & \cos\alpha\cos\beta & 0 \\ 0 & 0 & 2\cos\alpha \end{pmatrix}. \quad (18)$$

C. Deformation of the crystal field

There are two different ways the crystal field $V(\vec{r})$ is deformed from the ideal case $V(\vec{r}) \propto V_{\text{oct}}(\vec{r})$ when the octahedra are rigidly rotated.

(1) The relative rotations of the AB and O frames due to the rigid rotation and tilting of the oxygen octahedra removes the choice of a set of d orbitals where the effect of AB and O cages is the same. We no longer just get e_g, t_{2g} manifolds in any frame but with splittings induced by the rotation, which generates nonoctahedral but still only $l = 4$ field components.

(2) The rigid rotation and tilting of the octahedra keeps the octahedra symmetric but deforms the unit cell and AB ionic cages with it. This not only changes the $l = 4$ components but also induces $l = 2$ field components that can couple to the JT ion much more strongly [see discussion on D_2 versus D_4 below Eq. (12) in Sec. III A]. So, the magnitude of the net effect of the octahedral rotations is not limited by the relative sizes of the octahedral fields of AB and O in the cubic case (see Sec. IV A).

Since $V_O(\vec{r})$ is relatively stronger, we can take the octahedra's local frames (that are rotated with them) to first describe the effect of $V_O(\vec{r})$, i.e., splitting of degenerate d orbitals into e_g, t_{2g} manifolds with a gap Δ_o, and then consider the effect of $V_{AB}(\vec{r})$ on these manifolds. $V_{AB}(\vec{r})$ will couple and mix the orbitals in the two manifolds. Since $f_{q_A} \ll 1$, we can even ignore the coupling between the states belonging to different manifolds that are Δ_o apart. This also makes it possible to analytically solve the problem in two limiting cases discussed later.

It is worth reminding that $V(\vec{r})$ a scalar quantity in the position space but a vector in the spherical harmonics bases, so we can calculate it in one bases as per our convenience and then transform it to another.

$$V(\vec{r}) = \sum_{l,m} V_{lm} r^l Y_{lm}(\hat{r}) = \sum_{l,m} \tilde{V}_{lm} r^l \tilde{Y}_{lm}(\hat{r}), \quad (19)$$

$$\tilde{V}_{lm} = \sum_{m'=-l}^{l} \mathcal{R}_{m,m'}^l V_{lm'}, \quad (20)$$

where $\mathcal{R}^l = \mathcal{R}^l(\alpha, \beta)$ is the rotation matrix for real spherical harmonics of degree l. It can be calculated using the method devised by Ivanic and Ruedenberg [77]. The multipole components of $V_O(\vec{r})$ in the rotated frame do not change with the rigid octahedral rotations because, by definition, the octahedron itself rotates with its frame. These can be directly read off Eq. (3). Similarly, it is easier to obtain the components of $V_{AB}(\vec{r})$ in the unrotated frame so we do that first and later transforms them to obtain the rotated frame components. That is,

$$\tilde{V}_{lm} = \tilde{V}_{lm}^O + \sum_{m'=-l}^{l} \mathcal{R}_{mm'}^l V_{lm'}^{AB}, \quad (21)$$

$$V_{lm}^{AB} = \left(\frac{q_A}{a}\right) V_{lm}^A + \left(\frac{q_B}{a}\right) V_{lm}^B, \quad (22)$$

where the quantities bearing a tilde on top belong to the rotated (octahedron's) frame. As described above, $\tilde{V}_{lm}^O$ are simply octahedral field components with $l = 4$ and $m = 0, 4$ [see Eq. (3)]. However, V_{lm}^{AB} contain the effect of the deformation of the crystal structure so it now has not only other $l = 4$ components but also $l = 2$ components; see below. A procedure to obtain these multipole components, without actually calculating the projection of the potential $V_{AB}(\vec{r})$ onto the spherical harmonics, is described in the Appendix.

We find that the splittings due to octahedral rotation and tilting are practically the same for all B ions (but their eigenstates differ considerably, which creates interesting orbital ordering as discussed later in the discussion in Sec. VII), so we consider the octahedron 1 with central B ion at $\mathbf{a}/2$ in the calculations that follow. We obtain the following exact expressions for V_{lm}^A,

$$V_{2,-2}^A = 64\sqrt{\frac{3\pi}{5}} \cos^2\beta \left(\frac{1}{(\cos^2\alpha + 2\cos^2\beta)^{5/2}} - \frac{\sec^3\alpha}{(\cos 2\beta + 2)^{5/2}} \right), \quad (23)$$

$$V_{2,0}^A = 32\sqrt{\frac{\pi}{5}} \left(\frac{2\sec^3\alpha \sin^2\beta}{(\cos 2\beta + 2)^{5/2}} - \frac{32\sqrt{\frac{\pi}{5}}(\cos 2\beta - \cos 2\alpha)}{(\cos^2\alpha + 2\cos^2\beta)^{5/2}} \right), \quad (24)$$

$$V_{4,-2}^A = \frac{128\sqrt{5\pi}}{3} \cos^2\beta \left(\frac{3\cos 2\alpha - \cos 2\beta + 2}{(\cos^2\alpha + 2\cos^2\beta)^{9/2}} + \frac{\sec^5\alpha(\cos 2\beta - 5)}{(\cos 2\beta + 2)^{9/2}} \right), \quad (25)$$

$$V_{4,0}^A = \frac{16\sqrt{\pi}}{3} \left(\frac{\sec^5\alpha(36\cos 2\beta - 3\cos 4\beta + 23)}{(\cos 2\beta + 2)^{9/2}} - \frac{8\cos 2\alpha(3\cos 2\beta + 2) - 2\cos 4\alpha + 12\cos 2\beta - 3\cos 4\beta + 9}{(\cos^2\alpha + 2\cos^2\beta)^{9/2}} \right),$$

$$V_{4,4}^A = -\frac{128\sqrt{35\pi}}{3} \cos^4\beta \left(\frac{1}{(\cos^2\alpha + 2\cos^2\beta)^{9/2}} + \frac{\sec^5\alpha}{(\cos 2\beta + 2)^{9/2}} \right), \quad (26)$$

whereas V_{lm}^B are given by

$$V_{2,-2}^B = 64\sqrt{\frac{3\pi}{5}} \frac{\sin^2 \alpha \sec^3 \beta}{(\cos 2\alpha + 3)^{5/2}}, \tag{27}$$

$$V_{2,0}^B = 4\sqrt{\frac{\pi}{5}} \left(\sec^3 \alpha - \frac{8 \sec^3 \beta}{(\cos 2\alpha + 3)^{3/2}} \right), \tag{28}$$

$$V_{4,-2}^B = -\frac{128\sqrt{5\pi}}{3} \frac{\sin^2 \alpha \sec^5 \beta}{(\cos 2\alpha + 3)^{7/2}}, \tag{29}$$

$$V_{4,0}^B = \frac{4\sqrt{\pi}}{3} \left(\frac{24 \sec^5 \beta}{(\cos 2\alpha + 3)^{5/2}} + \sec^5 \alpha \right), \tag{30}$$

$$V_{4,4}^B = \frac{16\sqrt{35\pi}}{3} \frac{(20 \cos 2\alpha - \cos 4\alpha + 13) \sec^5 \beta}{(\cos 2\alpha + 3)^{9/2}}. \tag{31}$$

The Hamiltonian of the central ion (JT ion) including the crystal field of the AB cages in the octahedron's frame are given by

$$\tilde{H}_{m'm''} = \sum_{l,m} \tilde{V}_{lm} \tilde{C}_l^{m'm''m} D_l, \tag{32}$$

where $\tilde{C}_l^{m'm''m} = \langle \tilde{Y}_{2m'} | \tilde{Y}_{lm} | \tilde{Y}_{2m''} \rangle = C_l^{m'm''m}$.

V. RESULTS: SINGLE PARTICLE SPECTRUM AND JT INSTABILITY

Before we present our results, let us briefly describe the kind of behavior that would indicate a JT instab against the tilting and rotations of the octahedra, and how it relates to the standard JT problem. As describe in Sec. III, the optimum structure can have a finite distortion as long as the splitting in the single particle spectrum has a different dependence on the distortion than the elastic energy associated with the changes in the unit cell volume. Here, the unit cell volume depends on the "distortions" α, β as $v = 4a^3 \cos^2 \alpha \cos^2 \beta$, and, at $\alpha, \beta \ll 1$, it changes as $\sim a^3(\alpha^2 + \beta^2)$. The elastic energy in the harmonic approximation thus goes as $\sim(\alpha^2 + \beta^2)^2$, which is *quartic* in α, β. So, in contrast to the case of elongations or compressions of the octahedra [60], the behavior we are looking for in the electronic spectrum is not linear but quadratic, which would compete with such a quartic elastic energy to produce a finite distortion in the optimum structure. Thinking of squared angles α^2, β^2 as the basic distortion variables, the order of the electronic and elastic energy terms matches to the standard JT problem.

We will first focus on the t_{2g} manifold and see how the potential of the AB cages split it when the octahedra tilt and rotate.

A. t_{2g} manifold

Let's consider three cases separately, only rotation, only tilting, and both rotation and tilting.

1. Only rotation: $\alpha = 0$ and $\beta \neq 0$

Ignoring the coupling between the e_g and t_{2g} manifolds (between xy and $x^2 - y^2$ at $\alpha = 0$), their Hamiltonians turn out to be diagonal. We can write the single particle energies

of t_{2g} states as

$$(E_{xy}, E_{yz}, E_{zx}) = (2, -1, -1)[\Delta_2 D_2 + \Delta_4 D_4], \tag{33}$$

where E_{yz} and E_{zx} are degenerate and

$$\Delta_l = (q_A \Delta_l^A + q_B \Delta_l^B)/a, \ (l = 2, 4), \tag{34}$$

$$\Delta_2^A = \frac{64 \sin^2 \beta}{7(\cos 2\beta + 2)^{5/2}} \simeq \frac{64}{63\sqrt{3}} \beta^2, \tag{35}$$

$$\Delta_4^A = \frac{160 \sin^2 \beta}{63(\cos 2\beta + 2)^{9/2}}$$

$$\times (125 \cos 2\beta + 42 \cos 4\beta + 7 \cos 6\beta + 82) \tag{36}$$

$$\simeq \frac{40960}{5103\sqrt{3}} \beta^2, \tag{37}$$

$$\Delta_2^B = \frac{2}{7}(1 - \sec^3 \beta) \simeq -\frac{3}{7} \beta^2, \tag{38}$$

$$\Delta_4^B = \frac{5}{126}((7 \cos 4\beta - 3) \sec^5 \beta - 4) \simeq -\frac{115}{63} \beta^2. \tag{39}$$

We see that $\Delta_{2/4}^A > 0$ while $\Delta_{2/4}^B < 0$, revealing a competition between the two terms that would determine the sign and size of the term in the square bracket in Eq. (33) as q_A (and hence q_B) is varied. The average t_{2g} energy also shifts from $-2/5\Delta$ by an amount

$$E_0^{t_{2g}} = (q_A E_0^A + q_B E_0^B) D_4/a - (2/5) f_{q_A} \Delta_o, \tag{40}$$

where

$$E_0^A = \frac{8(92 \cos 2\beta + 24 \cos 4\beta + 20 \cos 6\beta + 5 \cos 8\beta + 51)}{9(\cos 2\beta + 2)^{9/2}}$$

$$\simeq \frac{512}{243\sqrt{3}} - \frac{2560\beta^2}{729\sqrt{3}}, \tag{41}$$

$$E_0^B = -\frac{1}{18}((5 \cos 4\beta + 3) \sec^5 \beta + 4)$$

$$\simeq -\frac{2}{3} + \frac{10\beta^2}{9}. \tag{42}$$

The results in Eqs. (33) and (40) are summarized in Fig. 2, where E_{xy}, $E_{yz/zx}$, and $E_0^{t_{2g}}$ are shown as a function of β at three values of $q_A/q_o = 1/2$ and 1, 2. We have assumed $D_2 = \sqrt{D_4}$ and taken $\Delta_o = 4q_o/15a$ throughout this paper, which fixes the value of $D_4 = 1/200$, and corresponds to $\Delta_o = 2.073$ eV at $q_o = 2$ e and $a = 7.0$ bohr. We present the energies as a percentage of Δ_o by calculating all quantities at the above values of q_o, a. Figure 2 shows that the competition between A and B cages determines the ground state and the size of the splitting between the t_{2g} states E_{xy} and $E_{yz/zx}$. In Fig. 2(a), where $q_A/q_o = 1/2$ ($q_B/q_o = 5/2$), the effect of B cage dominates. Since it's negative [see Eqs. (38) and (39)], it reverses the order in Eq. (33) and E_{xy} becomes lower than $E_{yz/zx}$, by about 6% of Δ_o at $\beta = 15°$. When A cage dominates at large q_A/q_o, as shown in Fig. 2(c) for $q_A/q_o = 2$, $E_{yz/zx}$ are the single particle ground states (with a splitting of the same order), whereas the net effect of both cages is reduced in Fig. 2(b) that corresponds to $q_A/q_o = 1$ and we only obtain a splitting of $\sim 2\%$ of Δ_o at $\beta = 15°$. Obviously, there will also be a point near $q_A/q_o = 1$ where A and B completely cancel the effect of each other (not shown in Fig. 2). We also see that
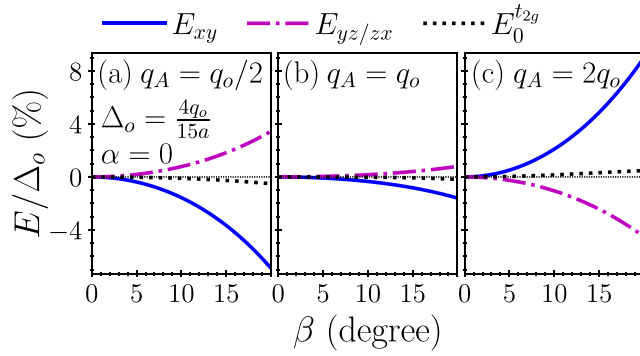
FIG. 2. Splitting in t_{2g} manifold induced by the octahedral rotations. E_{xy}, E_{yz}, E_{zx}, and $E_0^{t_{2g}}$ as a function of the rotation angel β at $\alpha = 0$ (no tilting), $\Delta_o = 4q_o/15a$ ($D_4 = 1/200$), $D_2 = \sqrt{D_4}$, and three values of q_A/q_o. (a) The B cage dominates at $q_A/q_o = 1/2$; it lowers xy state and raises yz, zx states with increasing β. As q_A/q_o increases to 1, (b) A cage almost cancels the effect of B cage reducing the splitting, while it dominates at $q_A/q_o = 2$ (c) where it switches the order of the states.

$E_0^{t_{2g}}$ changes from a small negative to a small positive value with an increase in q_A/q_o as we go from Fig. 2(a) to Fig. 2(c). This is because the rotation suppresses the effect of AB cages on the gap Δ between e_g and t_{2g}. Since A supports O while B opposes it, Δ slightly widens at small q_A and shrinks at large q_A, shifting the t_{2g} manifold slightly down or up with β.

These results also indicate that in case of a superlattice with q_A alternating between the two regimes shown in Figs. 2(a) and 2(c), we should obtain an alternating orbital order if the octahedra are rotated.

2. Only tilting: $\alpha \neq 0$ and $\beta = 0$

In this case, the situation gets slightly complicated as the couplings between the three states become finite. However, the Hamiltonian still has a simple structure,

$$\tilde{H} = \begin{pmatrix} E_{xy} & g & -g \\ g & E_{yz} & \lambda \\ -g & \lambda & E_{yz} \end{pmatrix}, \quad (43)$$

where the matrix elements have relatively long expressions and only an approximation at small α, β is given later in this section. $\tilde{H}$ can be simplified by rotating the bases in $\{|yz\rangle, |zx\rangle\}$ space to obtain bright and dark states as follows.

$$|B\rangle = (|yz\rangle - |zx\rangle)/\sqrt{2}, \quad (44)$$

$$|D\rangle = (|yz\rangle + |zx\rangle)/\sqrt{2}. \quad (45)$$

The state $|D\rangle$ at energy $E_D = E_{yz} + \lambda$ decouples from the rest (so is already an eigenstate of $\tilde{H}$) and the state $|B\rangle$ at energy $E_{yz} - \lambda$ obtains the enhanced collective coupling $\sqrt{2}g$. The Hamiltonian can thus be solved analytically to obtain the remaining two eigenstates

$$|+\rangle = \cos\gamma |xy\rangle + \sin\gamma |B\rangle, \quad (46)$$

$$|-\rangle = \sin\gamma |xy\rangle - \cos\gamma |B\rangle, \quad (47)$$

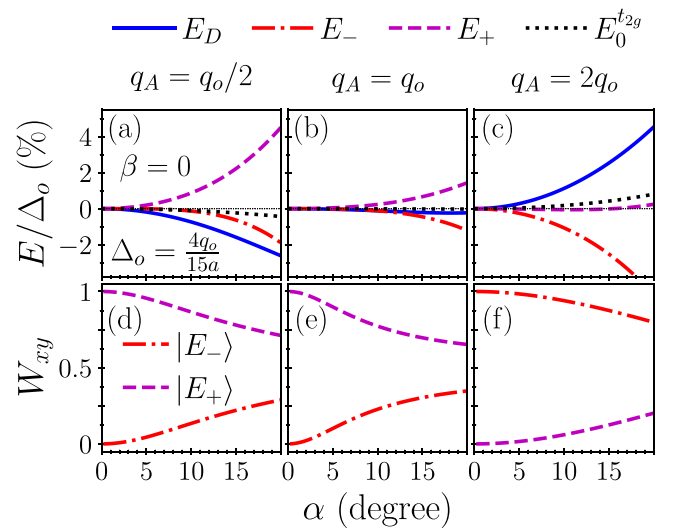$$\tan 2\gamma = \sqrt{8}g/(E_{xy} - E_{yz} + \lambda), \quad (48)$$

FIG. 3. Splitting and mixing in t_{2g} manifold induced by octahedral tilting. [(a)–(c)] E_D, $E_{\pm}$, and $E_0^{t_{2g}}$ as a function of α at $\beta = 0$; other parameters are the same as in Fig. 2. [(d)–(f)] Weight W_{xy} of xy orbital in $|E_{\pm}\rangle$ states shown in (a)–(c). The xy orbital predominantly contributes to $|E_+\rangle$ at $q_A/q_o = 1/2, 1$ [(a), (b), (d), and (e)], but to $|E_-\rangle$ at $q_A/q_o = 2$ [(c) and (f)].

at energies

$$E_{\pm} = \frac{E_{xy} + E_{yz} - \lambda}{2} \pm \frac{1}{2}\sqrt{(E_{xy} - E_{yz} + \lambda)^2 + 8g^2}. \quad (49)$$

Since we are only interested in small tilt and rotation, an expansion of the matrix elements of the Hamiltonian about $\alpha, \beta = 0$ to the leading order turns out to be quite good an approximation. The matrix elements in this case simplify a lot. Defining a vector $Q = (q_A D_2, q_A D_4, q_B D_2, q_B D_4)$, we can write them as

$$E_{xy} = Q \cdot \left(-\frac{64\alpha^2}{63\sqrt{3}}, -\frac{512(15\alpha^2 + 7)}{1701\sqrt{3}}, \frac{3\alpha^2}{7}, \frac{5\alpha^2}{7} + \frac{2}{3} \right), \quad (50)$$

$$E_{yz} = Q \cdot \left(\frac{32\alpha^2}{63\sqrt{3}}, \frac{512(25\alpha^2 - 7)}{1701\sqrt{3}}, -\frac{3\alpha^2}{14}, -\frac{85\alpha^2}{42} + \frac{2}{3} \right), \quad (51)$$

$$g = Q \cdot \left(-\frac{80}{63}\sqrt{\frac{2}{3}}\alpha^3, 0, \frac{15\alpha^3}{14\sqrt{2}}, \frac{5\alpha^3}{2\sqrt{2}} \right), \quad (52)$$

$$\lambda = Q \cdot \left(\frac{64\alpha^2}{63\sqrt{3}}, -\frac{2560\alpha^2}{1701\sqrt{3}}, -\frac{3\alpha^2}{7}, \frac{40\alpha^2}{21} \right). \quad (53)$$

E_D and $E_{\pm}$ relative to their average and the weight of xy state W_{xy} in $E_{\pm}$, as a function of α at $q_A/q_o = 1/2, 1, 2$ (and $\Delta_o = 4q_o/15a$) are shown in Fig. 3. The average shifts slightly with α, q_A by $E_0^{t_{2g}} = (E_{xy} + 2E_{yz})/3 - (2/5)f_{q_A}\Delta_o$, again reflecting a change in the gap Δ, and is also included in Fig. 3. Apart from the mixing between the three states xy, yz, zx in $|\pm\rangle$ at finite α, Fig. 3 shows a similar trend as in Fig. 2 but with an interesting twist. In contrast to $\alpha = 0$ case discussed in the previous section, W_{xy} is the
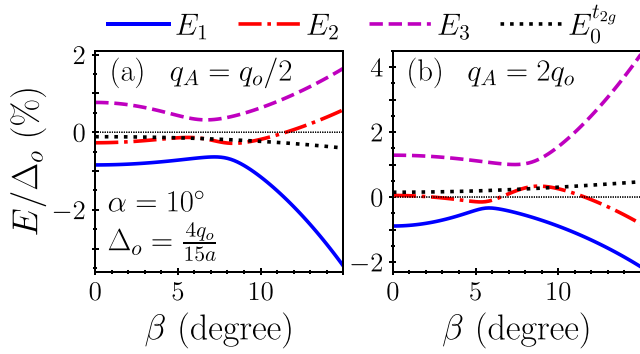
FIG. 4. Splitting in t_{2g} manifold due to octahedral rotation and tilting. t_{2g} energies as a function of β at $\alpha = 10°$ at the same values of other parameters as in Figs. 2 and 3. There are two anticrossings between the three states around $\beta \sim \alpha$. The character of the states depends on the competition between the two angles and the two ion cages.

largest in the highest (lowest) energy state at small (large) q_A/q_o, as shown in Figs. 3(a) and 3(c). α and β would thus tend to produce different ordering (details in the next section). The splittings are also about the same magnitude, between 4%–6% at $\alpha = 15°$ at $q_A/q_o = 1/2, 2$ [Figs. 3(a) and 3(c)] and about 2% at $q_A/q_o = 1$ [Fig. 3(b)]. The mixing is sizable but still far from perfect (50%/50%) even at the largest α shown ($W_{xy} = 0.25$–0.35 at $\alpha = 20°$). Overall, at finite α, the lowest energy state is either purely xy/yz, or contains at least some fraction of these, but it is never pure xy.

3. Rotation and tilting: $\alpha, \beta \neq 0$

The t_{2g} Hamiltonian in the general case $\alpha, \beta \neq 0$ cannot be solved analytically so there is no longer any advantage of ignoring the coupling between the e_g and t_{2g} manifolds. Even though their effect should be negligible due to a large gap Δ between the two manifolds, here we keep these couplings and numerically solve the full Hamiltonian. Figure 4 shows the energies at $\alpha = 10°$ as a function of β at $q_A/q_o = 1/2, 2$ and $\Delta_o = 4q_o/15a$ again. All states in the t_{2g} mix up to make the eigenstates $\{|E_i\rangle\}$ at energies $\{E_i\}$, $i = 1, 2, 3$. At $\beta = 0$, these results correspond to $\alpha = 10°$ in Figs. 3(a) and 3(c), so the lowest state at $\beta = 0$ here is $|D\rangle$ in Fig. 4(a) while it is the highest in Fig. 4(b). We see two anticrossings or level repulsion in either of Figs. 4(a,b) in different orders. In Fig. 4(a), the anticorssing between the highest two states occurs at smaller β, while the situation is the opposite in Fig. 4(b) where it occurs between the lowest pair at smaller β. From the results in the previous two sections, we know that not only A and B but also α and β tend to establish different orders. To get more insight, the weights of these three t_{2g} states in the three eigenstates are shown in Fig. 5. Let us first focus on the left column ($q_A/q_o = 1/2$). Figure 5(a) shows that, while $|E_1\rangle \to |D\rangle$ as $\beta \to 0$, $|E_1\rangle$ practically stays in yz, xz subspace for $\beta < 7°$ and it quickly becomes xy as $\beta \to \alpha = 10°$. Figures 5(b) and 5(c) show a complimentary behavior between xy and yz, xz, where $|E_3\rangle$ transforms from almost pure xy at $\beta = 0$ to almost complete yz, xz at $\beta \gtrsim \alpha = 10°$. The right column in Fig. 5 ($q_A/q_o = 2$), shows the
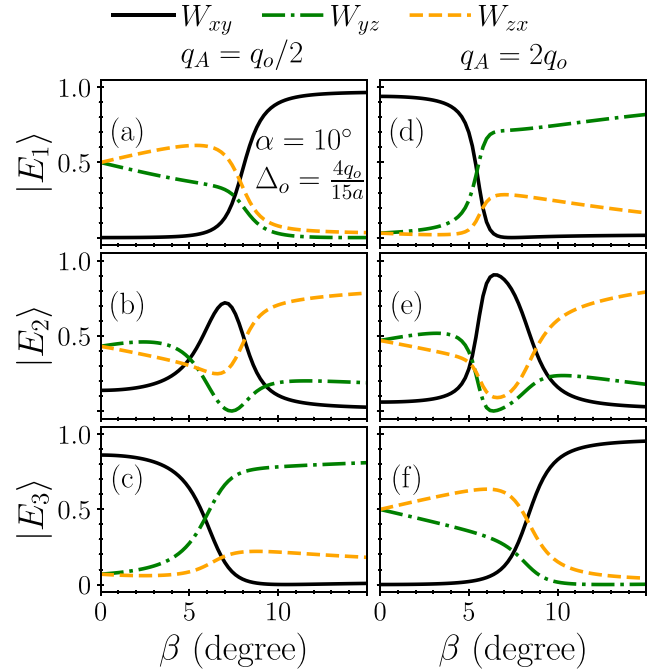

FIG. 5. The dependence of the character of the t_{2g} states on the competitions between α, β and A,B ion cages. Weights of the three t_{2g} orbitals in the three t_{2g} eigenstates shown in Fig. 4. At $q_A = q_o/2$, the B cage dominates and $|E_1\rangle$ is predominantly yz, zx at $\beta \sim 0 \ll \alpha = 10°$ but becomes $\sim xy$ at $\beta \gtrsim 10°$ (a). The situation flips when A cage dominates at $q_A = 2q_o$ (d). Similarly, the character of $|E_3\rangle$ at $q_A = q_o/2$ resembles that of $|E_1\rangle$ at $q_A = 2q_o$ [compare (c) with (d)] and vice versa [compare (f) with (a)]. The character of the middle state $|E_2\rangle$ [(b) and (e)] becomes $\sim xy$ only around the "resonance" region $\beta \sim \alpha$.

opposite behavior about the "resonance" $\beta \sim \alpha$. Figures 5(b) and 5(e) show an interesting aspect, the W_{xy} peaking in the middle state $|E_2\rangle$ before it is transferred between $|E_1\rangle$ and $|E_2\rangle$ around $\beta \sim \alpha$, i.e., at β between the two anticrossings in Fig. 4, which makes sense if we imagine the continuation of various energy surfaces/curves in the spectra in Fig. 4 ignoring their anticorssings: xy starts from the top and goes down in Fig. 4(a), while it starts from the bottom and goes up in Fig. 4(b).

In a given material, assuming the charges on A and B are fixed and either A or B dominates, one type of distortion would be energetically preferred over the other for certain numbers of electrons in the d orbitals of the Jahn-Teller ion B. For example, if B cage dominates, a d^2 configuration should prefer tilting over rotation because it stabilizes two occupied orbitals while rotation stabilizes one and destabilizes the other occupied orbital.

B. e_g manifold

Since e_g has only two states, we can always analytically diagonalize it if we ignore its coupling to the t_{2g} states. The expressions for the matrix elements of the Hamiltonian are long however, so we present the expansion at small angles in the following. The diagonal terms with reference to the

average e_g energy are given by

$$(H_{x^2-y^2}, H_{z^2}) = (1, -1)[\Omega_2 D_2 + \Omega_4 D_4], \tag{54}$$

$$\Omega_l = (q_A \Omega_l^A + q_B \Omega_l^B)/a, \quad (l = 2, 4), \tag{55}$$

$$\Omega_2^A = -\frac{64(\alpha^2(7\beta^2 + 3) - 6\beta^2)}{189\sqrt{3}}, \tag{56}$$

$$\Omega_4^A = \frac{640(\alpha^2(\beta^2 + 16) - 32\beta^2)}{1701\sqrt{3}}, \tag{57}$$

$$\Omega_2^B = \frac{3}{14}(\alpha^2(3\beta^2 + 2) - 4\beta^2), \tag{58}$$

$$\Omega_4^B = -\frac{5}{168}(\alpha^2(37\beta^2 + 46) - 92\beta^2), \tag{59}$$

whereas the coupling between the two states is

$$H_{x^2-y^2,z^2} = \frac{2\alpha^2\beta}{567}(128q_A(3D_2 - 20D_4) \\ - 81\sqrt{3}q_B(2D_2 - 5D_4)), \tag{60}$$

which vanishes if either of α, β is zero.

The average energy slightly shifts at nonzero α, β from $3/5\Delta$ by an amount

$$E_0^{e_g} = (q_A E_0^A + q_B E_0^B)D_4/a - (3/5)f_{q_A}\Delta_o, \tag{61}$$

$$E_0^A = \frac{256(5(4\beta^2 + 1)\alpha^2 + 5\beta^2 - 3)}{243\sqrt{3}}, \tag{62}$$

$$E_0^B = -\frac{1}{12}5(7\beta^2 + 4)\alpha^2 - \frac{5\beta^2}{3} + 1. \tag{63}$$

Diagonalising the Hamiltonian, we obtain two eigenstates $|\pm\rangle$ at energies $E_\pm$. We present the results obtained using the exact expressions instead of the expansions in Eqs. (54) and (60). Figure 6 shows $E_\pm$ and weights $W_{x^2-y^2}$ of $x^2 - y^2$ orbital in the two states as a function of β at $\alpha = 10°$, $\Delta_o = 4q_o/15a$, and $q_A/q_o = 1/2, 2$. We get the same ordering of orbitals "with and without z" as in t_{2g} case, i.e., at $q_A/q_o = 1/2$, β tends to lower $x^2 - y^2$ while α tend to lower z^2 orbital, as indicated by the behavior of $W_{x^2-y^2}$, which is almost zero in $|E_-\rangle$ at $\beta \lesssim 5°$ ($\ll \alpha = 10°$), while it approaches unity at $\beta \gtrsim \alpha$. Similarly, at $q_A/q_o = 2$, $W_{x^2-y^2}$ shows this behavior for $|E_+\rangle$. This is also evident from the signs of the Ω_l in Eq. (54). We see that $l = 2$ terms have the same signs as t_{2g} case but $l = 4$ terms have switched the signs. Since D_4 is much smaller than D_2, we will still get the same ordering as in t_{2g} case. The splitting is much smaller in this case though, only $\sim 0.5\%$ of Δ_o at $\beta = 10°$ in either case shown. To see how well the expansions in Eqs. (54) and (60) can approximate the exact results, Fig. 6 includes them as thin dotted lines that are collectively labeled Approx., which are almost indistinguishable from the exact results at $q_A/q_o = 1/2$, but deviate at $q_A/q_o = 2$ as their "resonance point" is shifted towards larger β.

C. Effect of the full lattice

In a crystal, obviously, not only the nearest coordination cages of A and B ions but also the other ions (including O) at longer distances all have finite contributions to the crystal field and hence the JT effect. To see how much our results change when the full lattice (FL) is considered instead of just
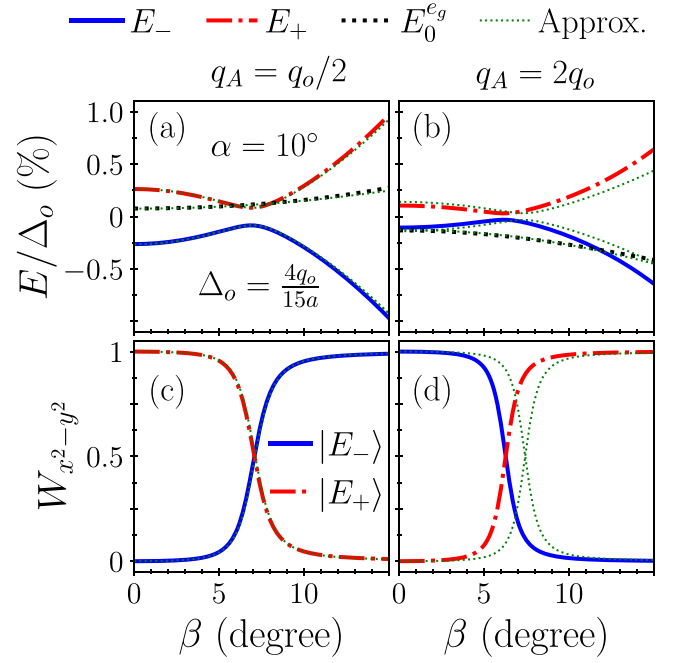

FIG. 6. Energies and characters of e_g states. $E_\pm$ and $E_0^{e_g}$ as a function of β at $\alpha = 10°$, and the same parameters as in Fig. 4. At $q_A = q_o/2$ [(a) and (c)] where B cage dominates, α tends to make $|E_+\rangle$ more $x^2 - y^2$ (see small β region), while β tends to do the opposite (see large β region). The roles of α, β switch at $q_A = 2q_o$ [(b) and (d)], where A cage dominates. We see that the splitting is relatively small as compared to t_{2g} manifold. Approximate results obtained by a second order expansion of the Hamiltonian given in Eqs. (54)–(61) are also shown for comparison.

the nearest AB cages, we numerically calculate the multipole components of the potential of the full lattice by following the recipe in Refs. [75,78,79] and Ewald summation method [80]. To do this, we borrow relevant routines from the tight binding package in Questaal suite [81] that implements these methods.

We find that the potential of the FL does not change the qualitative picture we presented but merely shifts the balance between A and B cages towards smaller q_A. This can be seen in Fig. 7 where the energies of the t_{2g} states as a function of q_A/q_o are compared for the two cases at $\alpha = 0$, $\beta = 20°$ (and $\Delta_o = 4q_o/15a$). In case of AB cages, the crossing of the (xy and yz/zx) energy levels occurs at $q_A/q_o \simeq 1.1$, whereas the FL moves it to $q_A/q_o \simeq 0.3$. The slopes of the lines are almost the same in both cases, meaning that the splitting due to octahedral rotations would be the same in both cases if q_A is measured from their crossing points. The shift towards smaller q_A in case of FL can be explained by noting that the next coordination cage beyond the first AB cages has O ions (24 of them at a distance of $\sqrt{5}a/2$ at $\alpha, \beta = 0$) that supports A cage against the B cage, lowering the value of q_A that balances it at the crossing in Fig. 7. It significantly increases the agreement between the two cases presented by moving the crossing point to $q_A/q_o \simeq 0.8$ (not shown in Fig. 7).

From the above results, we also see that a comparison between the rotation induced splittings in the two cases (FL versus AB cages) at a fixed value of q_A would show an underestimation or an overestimation depending on whether q_A
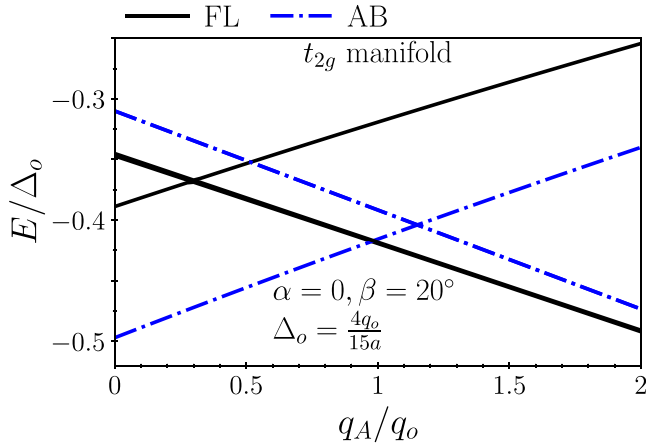
FIG. 7. The effect of the potential of full ionic lattice. t_{2g} spectrum computed using the potential of full lattice and that obtained from only nearest AB cages (and the anion octahedron itself) are shown as a function of q_A/q_o at $\alpha = 0$, $\beta = 20°$, and $\Delta_o = 4q_o/15a$. Full lattice only shifts the balance between the two cation cages towards A (i.e, the crossing point, where the two cages balance each other, moves to smaller q_A) but keeps the qualitative picture the same. (The bold black line is nothing but an overlap of two practically degenerate black lines.)

lies to the right or the left side of the middle point of the two crossings. Besides, the characters of the eigenstates would be in a disagreement at q_A between the two crossings.

VI. SUMMARY AND CONCLUSION

We consider the effects of octahedral rotations and tilting in perovskites on the t_{2g} and e_g manifolds of the central transition metal ions. We find significant splitting in these levels caused by the distortions in the crystal field of nearest A and B ion cages, which essentially amounts to a Jahn-Teller instability. The sign and strength of this effect is determined by a competition between the two ion cages. The tilt and rotation also tend to establish different ground states depending on which ion cage dominates. While the tilting alone can mix t_{2g} states, e_g states do not mix unless both rotation and tilting are nonzero. Despite such mixing, we can see which orbitals are stabilized or destabilized. If A cage dominates (i.e., q_A is larger than a critical value), tilting lowers $xy, x^2 - y^2$ orbitals and raises yz, zx, z^2, while rotation tends to do the opposite; the whole situation reverses if B cage dominates. Considering the crystal field of the full lattice only shifts the balance towards A cage but does not qualitatively change the results.

VII. DISCUSSION AND OUTLOOK

We have only focused on the spectrum of the B ion at $\mathbf{a}/2$ in the cell described in Sec. IV B but there are three more *distinct* B ions in the unit cell at finite octahedral rotations that also need to be considered simultaneously. We find that the splittings in the spectra of all B ions are practically identical. However, their eigenstates are different in a way that can create interesting orbital ordering that depends on the tilt and rotation angles, unlike what happens in tetragonal Jahn-Teller
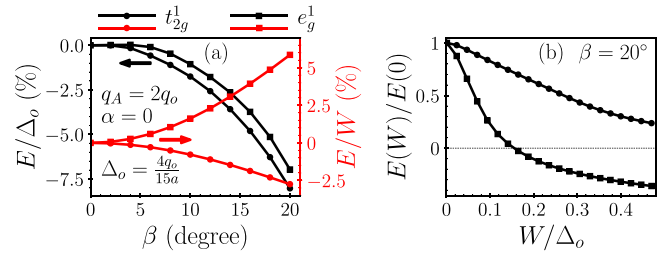

FIG. 8. The effect of electron hopping between B sites. (a) Energy of two configurations t_{2g}^1 and e_g^1 as a function of β when either the crystal field or the hopping is considered alone. In the latter case, the energy changes are scaled with the bandwidth W. (b) Considering both the crystal field and the hopping simultaneously, the ratio of the change in energy with rotation β at a finite hopping to that in the absence of hopping $E(W)/E(0)$ as a function of the average bandwidth W, for the same two configurations t_{2g}^1 and e_g^1. The results of the crystal field model presented in this manuscript hold in the small bandwidth limit where $E(W)/E(0) \sim 1$.

distortions (elongation and compression) such as seen in KCuF$_3$ [82], where the orbital ordering does not depend on the size of the distortion. The eigenstates' components in the local bases attached to the octahedra's frame also vary between different B sites so the dependence on the rotation and tilt angle is not trivial, which is understandable because different B sites in the unit cell have different environments. A detailed study of orbital ordering in this case is out of scope of this manuscript and is left for future work.

Of course, beside the crystal field we consider in our simplistic model, in real materials, there would be other local effects like electronic correlations (Hubbard and Hund's interaction) and spin-orbit interaction, as well as band structure effects arising from the electron hopping between the B ions. The interplay between these and the crystal field (or JT) effect we discussed in this manuscript is also an interesting future work. A discussion about the role of electron hopping along with some preliminary results follows.

Assuming the crystal field splitting to be the largest energy scale, the orbitals in the e_g and t_{2g} manifolds of B sites are aligned with their respective octahedra. The electron hopping between these orbitals that are localized on different B sites depends on the relative orientation of the orbitals. As the octahedra rotate (or tilt), the hybridization between the neighboring sites change, modifying the electronic bands and associated band energy.

To shed some light on the role of these band structure effects, we consider the nearest neighbor hopping between the B sites using the Slater-Koster method [83] and calculate the change in the energy of the system as the octahedra rotate. We do this for three cases: with either the crystal field or the hopping only, and with both of these simultaneously. Figure 8(a) shows the change in the energy of two (spinless) configurations t_{2g}^1 and e_g^1 as a function of β for the first two cases for the crystal-field-only (black curves, left y axis; $\alpha = 0$, $q = 2q_o$, $\Delta_o = 4q_o/15a$) and for the hopping-only case (red/gray curves, right y axis). We use Slater-Koster hopping parameters $(t_\sigma, t_\pi, t_\delta) = (0.15, -0.1, 0.025)$ eV, $a = 7$ bohr, $q_o = 2$ e, and consider only the crystal field of O octahedra that creates

t_{2g} and e_g manifolds. (These parameters produce an average bandwidth $W = 0.97$ eV for the two manifolds). While both t_{2g}^1 and e_g^1 configurations show a lowering of energy due to the crystal field as β increases—consistent with the results presented before—the energy of e_g^1 increases when only hopping is considered (the effect scales with the hopping parameters or the bandwidth). This is due to a reduced hybridization leading to narrower e_g bands. In contrast, the energy of t_{2g}^1 decreases due to a band widening arising from an enhanced hybridization. The crystal field and these band structure effects are not additive however. The rotation induced splitting of the t_{2g}/e_g manifolds arising from the crystal field suppresses the effectiveness of the hopping in creating the dispersion in the energy states, and thus reduces the bandwidths and the the associated rotation induced energetic changes.

To show the validity regime of our crystal field model presented in this manuscript, Fig. 8(b) presents the ratio of the change in the energy at $\beta = 20°$ (i.e., the energy difference from the cubic case) at finite hopping $E(W)$ to that of our simplistic crystal field model $E(0)$ as a function of the average bandwidth W of t_{2g} and e_g bands. Here we scale the Slater-Koster parameters used for Fig. 8(a) to tune the bandwidth W. We see that $E(W)/E(0)$ decreases from unity at $W = 0$ to half its value for t_{2g}^1 configuration at $W/\Delta_o \gtrsim 0.3$, and even becomes negative for e_g^1 configuration around $W/\Delta_o \gtrsim 0.15$ (showing the dominance of the band structure effects). From this analysis, we conclude that the results of our crystal field model hold unambiguously only for narrower bands, $W/\Delta_o \ll 1$, while a detailed further study is required to understand the interplay of the two effects at larger bandwidths.

APPENDIX: COMPUTING V_{lm}

Here we describe a method to obtain the multipole components V_{lm} of a potentials $V(\vec{r})$ at a position $\vec{r}$ around a JT ion. It is worth noting that this can be done without evaluating the inner products between the spherical harmonics and $V(\vec{r})$.

Let's consider $V^A(\vec{r})$ to illustrate the idea. $V^B(\vec{r})$ and $V^{JT}(\vec{r})$ can also be dealt in the same way. We like to expand the potentials $V^A(\vec{r})$ in spherical harmonics as

$$V^A(\vec{r}) = \frac{q_A}{a} \sum_{l,m} V_{lm}^A \left(\frac{r}{a}\right)^l Y_{lm}(\hat{r}), \tag{A1}$$

where we have assumed a as a length scale and taken out the factor q_A/a for clarity.

First we calculate $V^A(\vec{r})$ using the simple textbook formula. $V^A(\vec{r}; \alpha, \beta) = q_A \sum_i 1/|\vec{r}_i^A - \vec{r}|$, where $\vec{r}_i^A$ is the position of ith A ion and $\vec{r}$ is the position of the observation point measured from the JT ion. Writing Cartesian components of $\vec{r}$ as $\vec{r} = r(\cos\phi\sin\theta, \sin\theta\sin\phi, \cos\theta)$, where (r, θ, ϕ) are the spherical coordinates in the frame of JT ion and expanding $V^A(\vec{r}; \alpha, \beta)$ in powers of r, we can separate coefficient of r^l that give degree l components. We can then consider each degree l term individually, and resolve it in its $(2l + 1)$ m components. This can be done by expanding such a coefficient of r^l in powers of $\cos\theta$, $\cos\phi$ (or $\sin\theta$, $\sin\phi$) and comparing the terms with a similar expansion of the formal expression on the right side of Eq. (A1). This gives a set of linear equations in $\{V_{lm}^A\}$ (for a fixed value of l) that can be easily solved. The whole calculation can be performed on MATHEMATICA [84] or a similar software.

[1] P. Zubko, S. Gariglio, M. Gabay, P. Ghosez, and J.-M. Triscone, Interface physics in complex oxide heterostructures, Annu. Rev. Condens. Matter Phys. **2**, 141 (2011).

[2] H. Y. Hwang, Y. Iwasa, M. Kawasaki, B. Keimer, N. Nagaosa, and Y. Tokura, Emergent phenomena at oxide interfaces, Nat. Mater. **11**, 103 (2012).

[3] A. Bhattacharya and S. J. May, Magnetic oxide heterostructures, Annu. Rev. Mater. Res. **44**, 65 (2014).

[4] F. Hellman, A. Hoffmann, Y. Tserkovnyak, G. S. D. Beach, E. E. Fullerton, C. Leighton, A. H. MacDonald, D. C. Ralph, D. A. Arena, H. A. Dürr, P. Fischer, J. Grollier, J. P. Heremans, T. Jungwirth, A. V. Kimel, B. Koopmans, I. N. Krivorotov, S. J. May, A. K. Petford-Long, J. M. Rondinelli *et al.*, Interface-induced phenomena in magnetism, Rev. Mod. Phys. **89**, 025006 (2017).

[5] H. Chen and A. Millis, Charge transfer driven emergent phenomena in oxide heterostructures, J. Phys.: Condens. Matter **29**, 243001 (2017).

[6] E. Dagotto, Complexity in strongly correlated electronic systems, Science **309**, 257 (2005).

[7] E. Dagotto and Y. Tokura, Strongly correlated electronic materials: Present and future, MRS Bull. **33**, 1037 (2008).

[8] M. B. Salamon and M. Jaime, The physics of manganites: Structure and transport, Rev. Mod. Phys. **73**, 583 (2001).

[9] J. Wang, J. B. Neaton, H. Zheng, V. Nagarajan, S. B. Ogale, B. Liu, D. Viehland, V. Vaithyanathan, D. G. Schlom, U. V. Waghmare, N. A. Spaldin, K. M. Rabe, M. Wuttig, and R. Ramesh, Epitaxial BiFeO$_3$ multiferroic thin film heterostructures, Science **299**, 1719 (2003).

[10] M. Dawber, K. M. Rabe, and J. F. Scott, Physics of thin-film ferroelectric oxides, Rev. Mod. Phys. **77**, 1083 (2005).

[11] D. G. Schlom, L.-Q. Chen, C.-B. Eom, K. M. Rabe, S. K. Streiffer, and J.-M. Triscone, Strain tuning of ferroelectric thin films, Annu. Rev. Mater. Res. **37**, 589 (2007).

[12] G. Koster, L. Klein, W. Siemons, G. Rijnders, J. S. Dodge, C.-B. Eom, D. H. A. Blank, and M. R. Beasley, Structure, physical properties, and applications of SrRuO$_3$ thin films, Rev. Mod. Phys. **84**, 253 (2012).

[13] I. B. Bersuker, The Jahn-Teller effect in crystal chemistry and spectroscopy, Coord. Chem. Rev. **14**, 357 (1975).

[14] K. I. Kugel and D. I. Khomskǐ, The jahn-teller effect and magnetism: Transition metal compounds, Sov. Phys. Usp. **25**, 231 (1982).

[15] A. J. Millis, Lattice effects in magnetoresistive manganese perovskites, Nature (London) **392**, 147 (1998).

[16] K. Terakura, Magnetism, orbital ordering and lattice distortion in perovskite transition-metal oxides, Prog. Mater. Sci. **52**, 388 (2007).

[17] M. A. Halcrow, Jahn–teller distortions in transition metal compounds, and their importance in functional molecular and inorganic materials, Chem. Soc. Rev. **42**, 1784 (2013).

[18] M. W. Lufaso and P. M. Woodward, Jahn–Teller distortions, cation ordering and octahedral tilting in perovskites, Acta Cryst. B **60**, 10 (2004).

[19] A. Glazer, Classification of tilted octahedra in perovskites, Acta Cryst. B **28**, 3384 (1972).

[20] N. W. Thomas, The compositional dependence of octahedral tilting in orthorhombic and tetragonal perovskites, Acta Cryst. B **52**, 16 (1996).

[21] P. M. Woodward, Octahedral Tilting in Perovskites. I. Geometrical Considerations, Acta Cryst. B **53**, 32 (1997).

[22] P. M. Woodward, Octahedral Tilting in Perovskites. II. Structure Stabilizing Forces, Acta Cryst. B **53**, 44 (1997).

[23] C. J. Howard and H. T. Stokes, Group-Theoretical Analysis of Octahedral Tilting in Perovskites, Acta Cryst. B **54**, 782 (1998).

[24] H. T. Stokes, E. H. Kisi, D. M. Hatch, and C. J. Howard, Group-theoretical analysis of octahedral tilting in ferroelectric perovskites, Acta Cryst. B **58**, 934 (2002).

[25] R. J. Angel, J. Zhao, and N. L. Ross, General rules for predicting phase transitions in perovskites due to octahedral tilting, Phys. Rev. Lett. **95**, 025503 (2005).

[26] P. Ghosez and J.-M. Triscone, Coupling of three lattice instabilities, Nat. Mater. **10**, 269 (2011).

[27] J. M. Rondinelli and C. J. Fennie, Octahedral rotation-induced ferroelectricity in cation ordered perovskites, Adv. Mater. **24**, 1961 (2012).

[28] J. T. Schick, L. Jiang, D. Saldana-Greco, and A. M. Rappe, Coupling between octahedral rotations and local polar displacements in WO_3/ReO_3 superlattices, Phys. Rev. B **89**, 195304 (2014).

[29] H. Sim and B. G. Kim, Octahedral tilting and ferroelectricity in $RbANb_2O_7$ ($a = $ Bi, Nd) from first principles, Phys. Rev. B **89**, 144114 (2014).

[30] M. H. Lee, C.-P. Chang, F.-T. Huang, G. Y. Guo, B. Gao, C. H. Chen, S.-W. Cheong, and M.-W. Chu, Hidden antipolar order parameter and entangled néel-type charged domain walls in hybrid improper ferroelectrics, Phys. Rev. Lett. **119**, 157601 (2017).

[31] H. Wang, F. Tang, M. Stengel, H. Xiang, Q. An, T. Low, and X. Wu, Convert widespread paraelectric perovskite to ferroelectrics, Phys. Rev. Lett. **128**, 197601 (2022).

[32] Y. Zhou, S. Dong, C. Shan, K. Ji, and J. Zhang, Two-dimensional ferroelectricity induced by octahedral rotation distortion in perovskite oxides, Phys. Rev. B **105**, 075408 (2022).

[33] L. Gao, C. Paillard, and L. Bellaiche, Photoinduced control of ferroelectricity in hybrid-improper ferroelectric superlattices, Phys. Rev. B **107**, 104109 (2023).

[34] D. Khomskii, Classifying multiferroics: Mechanisms and effects, Physics **2**, 20 (2009).

[35] N. A. Benedek and C. J. Fennie, Hybrid improper ferroelectricity: A mechanism for controllable polarization-magnetization coupling, Phys. Rev. Lett. **106**, 107204 (2011).

[36] Y. Yang, J. Íñiguez, A.-J. Mao, and L. Bellaiche, Prediction of a novel magnetoelectric switching mechanism in multiferroics, Phys. Rev. Lett. **112**, 057202 (2014).

[37] F. Ye, J. Wang, J. Sheng, C. Hoffmann, T. Gu, H. J. Xiang, W. Tian, J. J. Molaison, A. M. dos Santos, M. Matsuda, B. C. Chakoumakos, J. A. Fernandez-Baca, X. Tong, B. Gao, J. W. Kim, and S.-W. Cheong, Soft antiphase tilt of oxygen octahedra in the hybrid improper multiferroic $Ca_3Mn_{1.9}Ti_{0.1}O_7$, Phys. Rev. B **97**, 041112(R) (2018).

[38] J. Zhang, X. Shen, Y. Wang, C. Ji, Y. Zhou, J. Wang, F. Huang, and X. Lu, Design of two-dimensional multiferroics with direct polarization-magnetization coupling, Phys. Rev. Lett. **125**, 017601 (2020).

[39] Y. Zhang, J. Wang, and P. Ghosez, Unraveling the suppression of oxygen octahedra rotations in $A_3B_2O_7$ ruddlesden-popper compounds: Engineering multiferroicity and beyond, Phys. Rev. Lett. **125**, 157601 (2020).

[40] Y. Zhou, Z. Chen, Z. Wu, X. Shen, J. Wang, J. Zhang, and H. Sun, Hybrid improper ferroelectricity and magnetoelectric coupling in a two-dimensional perovskite oxide, Phys. Rev. B **103**, 224409 (2021).

[41] J. Zhang, Y. Zhou, F. Wang, X. Shen, J. Wang, and X. Lu, Coexistence and coupling of spin-induced ferroelectricity and ferromagnetism in perovskites, Phys. Rev. Lett. **129**, 117603 (2022).

[42] A. Amat, E. Mosconi, E. Ronca, C. Quarti, P. Umari, Md. K. Nazeeruddin, M. Gratzel, and F. De Angelis, Cation-induced band-gap tuning in organohalide perovskites: Interplay of spin-orbit coupling and octahedra tilting, Nano Lett. **14**, 3608 (2014).

[43] S. Krach, N. Forero-Correa, R.-I. Biega, S. E. Reyes-Lillo, and L. Leppert, Emergence of rashba-/dresselhaus effects in ruddlesden popper halide perovskites with octahedral rotations, J. Phys.: Condens. Matter **35**, 174001 (2023).

[44] P. V. Balachandran and J. M. Rondinelli, Interplay of octahedral rotations and breathing distortions in charge-ordering perovskite oxides, Phys. Rev. B **88**, 054101 (2013).

[45] P. Aguado-Puente, P. García-Fernández, and J. Junquera, Interplay of couplings between antiferrodistortive, ferroelectric, and strain degrees of freedom in monodomain $PbTiO_3/SrTiO_3$ superlattices, Phys. Rev. Lett. **107**, 217601 (2011).

[46] J. Jia, X. He, A. Akhtar, G. Herranz, and M. Pruneda, Dynamic control of octahedral rotation in perovskites by defect engineering, Phys. Rev. B **105**, 224112 (2022).

[47] H. J. Xiang, M. Guennou, J. Íñiguez, J. Kreisel, and L. Bellaiche, Rules and mechanisms governing octahedral tilts in perovskites under pressure, Phys. Rev. B **96**, 054102 (2017).

[48] R. D. Johnson, D. D. Khalyavin, P. Manuel, L. Zhang, K. Yamaura, and A. A. Belik, Emergence of a magnetostructural dipolar glass in the quadruple perovskite $dy_{1-\delta}mn_{7+\delta}o_{12}$, Phys. Rev. Lett. **125**, 097601 (2020).

[49] N. Ogawa, Y. Ogimoto, Y. Ida, Y. Nomura, R. Arita, and K. Miyano, Polar antiferromagnets produced with orbital order, Phys. Rev. Lett. **108**, 157603 (2012).

[50] L. Chen, C. Xu, H. Tian, H. Xiang, J. Íñiguez, Y. Yang, and L. Bellaiche, Electric-field control of magnetization, jahn-teller distortion, and orbital ordering in ferroelectric ferromagnets, Phys. Rev. Lett. **122**, 247701 (2019).

[51] W. Huang, W. Liu, Y.-C. Shao, X. Feng, N. Zhang, J. Fu, J.-M. Lee, D. Shen, Y.-D. Chuang, and X. Liu, Enhanced orbital anisotropy through the proximity to a $SrTio_3$ layer in the perovskite iridate superlattices, Phys. Rev. B **104**, 075156 (2021).

[52] E. Abarca Morales, G.-R. Siemann, A. Zivanovic, P. A. E. Murgatroyd, I. Marković, B. Edwards, C. A. Hooley, D. A. Sokolov, N. Kikugawa, C. Cacho, M. D. Watson, T. K. Kim,

C. W. Hicks, A. P. Mackenzie, and P. D. C. King, Hierarchy of lifshitz transitions in the surface electronic structure of sr_2ruo_4 under uniaxial compression, Phys. Rev. Lett. **130**, 096401 (2023).

[53] M. A. Carpenter and C. J. Howard, Symmetry rules and strain/order-parameter relationships for coupling between octahedral tilting and cooperative Jahn–Teller transitions in ABX_3 perovskites. I. Theory, Acta Cryst. B **65**, 134 (2009).

[54] H. A. Jahn, E. Teller, and F. G. Donnan, Stability of polyatomic molecules in degenerate electronic states - i—orbital degeneracy, Proc. R. Soc. A **161**, 220 (1937).

[55] H. A. Jahn and W. H. Bragg, Stability of polyatomic molecules in degenerate electronic states ii-spin degeneracy, Proc. R. Soc. A **164**, 117 (1938).

[56] U. Öpik and M. H. L. Pryce, Studies of the jahn-teller effect. i. a survey of the static problem, Proc. R. Soc. A **238**, 425 (1957).

[57] M. D. Sturge, *The Jahn-Teller Effect in Solids* (Academic Press, New York, 1968), pp. 91–211.

[58] G. A. Gehring and K. A. Gehring, Co-operative Jahn-Teller Effects, Rep. Prog. Phys. **38**, 1 (1975).

[59] E. Pavarini, in *Quantum Materials: Experiments and Theory*, edited by E. Pavarini, E. Koch, J. van den Brink, and G. Sawatzky, Schriften des Forschungszentrums Jülich. Reihe modeling and simulation (Forschungszentrum Jülich GmbH Zentralbibliothek, Verlag, Jülich, 2016), Vol. 6, p. 420 S.

[60] D. I. Khomskii and S. V. Streltsov, Orbital effects in solids: Basics, recent progress, and opportunities, Chem. Rev. **121**, 2992 (2021).

[61] V. Goldschmidt, The laws of crystal chemistry, Naturwissenschaften **14**, 477 (1926).

[62] G. Kieslich, S. Sun, and A. K. Cheetham, An extended tolerance factor approach for organic-inorganic perovskites, Chem. Sci. **6**, 3430 (2015).

[63] P. Garcia-Fernandez, J. a. Aramburu, M. T. Barriuso, and M. Moreno, Key role of covalent bonding in octahedral tilting in perovskites, J. Phys. Chem. Lett. **1**, 647 (2010).

[64] A. Cammarata and J. M. Rondinelli, Covalent dependence of octahedral rotations in orthorhombic perovskite oxides, J. Chem. Phys. **141**, 114704 (2014).

[65] J.-H. Lee, N. C. Bristowe, J. H. Lee, S.-H. Lee, P. D. Bristowe, A. K. Cheetham, and H. M. Jang, Resolving the physical origin of octahedral tilting in halide perovskites, Chem. Mater. **28**, 4259 (2016).

[66] S. Yoshida, H. Akamatsu, and K. Hayashi, Electronic origin of non-zone-center phonon condensation: Octahedral rotation as a case study, Phys. Rev. Lett. **127**, 215701 (2021).

[67] G. Herzberg and E. Teller, Schwingungsstruktur der elektronenübergänge bei mehratomigen molekülen, Z. Physik. Chem. **21B**, 410 (1933).

[68] I. B. Bersuker, On the origin of ferroelectricity in perovskite-type crystals, Phys. Lett. **20**, 589 (1966).

[69] N. Kristoffel and P. Konsin, Pseudo-jab-teller effect and second order phase transitions in crystals, Phys. Status Solidi B **21**, K39 (1967).

[70] R. G. Pearson, The second-order Jahn-Teller effect, J. Mol. Struct.: THEOCHEM **103**, 25 (1983).

[71] R. L. Fulton and M. Gouterman, Vibronic Coupling. I. Mathematical treatment for two electronic states, J. Chem. Phys. **35**, 1059 (1961).

[72] I. B. Bersuker, Pseudo-jahn teller effect: A two-state paradigm in formation, deformation, and transformation of molecular systems and solids, Chem. Rev. **113**, 1351 (2013).

[73] H. Bethe, Termaufspaltung in kristallen, Ann. Phys. **395**, 133 (1929).

[74] J. H. Van Vleck, Theory of the variations in paramagnetic anisotropy among different salts of the iron group, Phys. Rev. **41**, 208 (1932).

[75] A. T. Paxton, in *Multiscale Simulation Methods in Molecular Sciences*, edited by J. Grotendorst, N. Attig, S. Blügel, and D. Marx (Academic Press, Institute for Advanced Simulation, Forschungszentrum Jülich, 2009), Vol. 42, pp. 145–176.

[76] J.-M. Carter, V. V. Shankar, M. A. Zeb, and H.-Y. Kee, Semimetal and topological insulator in perovskite iridates, Phys. Rev. B **85**, 115105 (2012).

[77] J. Ivanic and K. Ruedenberg, Rotation matrices for real spherical harmonics. direct determination by recursion, J. Phys. Chem. **100**, 6342 (1996).

[78] M. W. Finnis, A. T. Paxton, M. Methfessel, and M. van Schilfgaarde, Crystal structures of zirconia from first principles and self-consistent tight binding, Phys. Rev. Lett. **81**, 5149 (1998).

[79] A. T. Paxton and M. W. Finnis, Magnetic tight binding and the iron-chromium enthalpy anomaly, Phys. Rev. B **77**, 024428 (2008).

[80] P. P. Ewald, Die berechnung optischer und elektrostatischer gitterpotentiale, Ann. Phys. **369**, 253 (1921).

[81] T. Paxton, TBE code (2009).

[82] A. I. Liechtenstein, V. I. Anisimov, and J. Zaanen, Density-functional theory and strong interactions: Orbital ordering in Mott-Hubbard insulators, Phys. Rev. B **52**, R5467 (1995).

[83] J. C. Slater and G. F. Koster, Simplified lcao method for the periodic potential problem, Phys. Rev. **94**, 1498 (1954).

[84] Wolfram Research, Inc., Mathematica, Version 13.3, champaign, IL, 2023.